Frequency-constrained Unit Commitment Considering Typhoon-induced Wind Farm Cutoff and Grid Islanding Events

Yanqi Liu, *Graduate Student Member*, *IEEE*, Dunjian Xie, *Member*, *IEEE*, and Hongcai Zhang, *Senior Member*, *IEEE*

***Abstract*—In coastal regions of China, offshore wind farm expansion has spurred extensive research to reduce operational costs in power systems with high penetration of wind power. However, frequent extreme weather conditions such as typhoons pose substantial challenges to system stability and security. Previous research has intensively examined the steady-state operations arising from typhoon-induced faults, with a limited emphasis on the transient frequency dynamics inherent to such faults. To address this challenge, this paper proposes a frequency-constrained unit commitment model that can promote energy utilization and improve resilience. The proposed model analyzes uncertainties stemming from transmission line failures and offshore wind generation through typhoon simulations. Two types of power disturbances resulting from typhoon-induced wind farm cutoff and grid islanding events are revealed. In addition, new frequency constraints are defined considering the changes in the topology of the power system. Further, the complex frequency nadir constraints are incorporated into a two-stage stochastic unit commitment model using the piecewise linearization. Finally, the proposed model is verified by numerical experiments, and the results demonstrate that the proposed model can effectively enhance system resilience under typhoons and improve frequency dynamic characteristics following fault disturbances.**

***Index Terms*—Frequency constraint, offshore wind farm, typhoon uncertainty, unit commitment.**

I. Introduction

In light of environmental deterioration and increasing concerns on energy security, China has embarked on planning an advanced power system dominated by wind energy, photovoltaic energy, and other renewable energy sources with the aim of peaking carbon dioxide emissions by 2030 and achieving carbon neutrality by 2060. The related studies have shown that China has abundant wind energy resources capable of harvesting 12900-15000 TWh of wind energy annually [1]. Wind power generation is typically categorized based on its installation location into onshore and offshore types. In the past decade, onshore wind power generation has experienced rapid development due to its easy installation and maintenance processes. However, constrained by its potential, the onshore wind power development is approaching a saturation level. In contrast, offshore wind power generation has a great untapped potential since the average wind resource in the coastal areas is much greater than the onshore one and is closer to the population-dense regions. For example, Guangdong Province, China has a potential offshore wind energy of 1584.4 TWh [2]. The annual growth rate of installed capacity for offshore wind power is 6.3%, and the newly added capacity is expected to reach 30 GW by 2027 [3].

As climate change progresses, there have been frequent extreme weather events such as floods and typhoons [4]. The power systems with offshore wind farms are susceptible to destructive impacts from typhoons in coastal areas of China [5]. Therefore, system operators tended to shut down offshore wind farms to prevent damages during typhoons, resulting in significant energy wastage. For example, when Typhoon Ampil hit Jiangsu Province, China, in 2017, wind generation increased to 1560000 kWh, thus almost doubling the output observed under normal operational conditions [6]. In recent years, certain advancements have been made in the anti-typhoon design of offshore wind turbines; for example, the 5.5 MW typhoon-resistant floating offshore wind turbines have been developed [3]. By employing control strategies of the pitch and yaw systems, the wind load on the turbine during a typhoon can be reduced, ensuring structural safety and functional integrity [7]. Despite the potential threats of typhoons, the power system operators aim to enlarge wind power generation and improve the power system resilience during typhoons through reasonable operation and application of control strategies [8]. Hence, the objective of this study is to develop a proactive unit commitment strategy aimed at improving the utilization of offshore wind resources and system resilience under typhoon conditions.

For power systems with high penetration of offshore wind

Manuscript received: January 28, 2024; revised: April 1, 2024; accepted: May 22, 2024. Date of CrossCheck: May 22, 2024. Date of online publication: June 11, 2024.

This paper was supported by the Science and Technology Development Fund, Macau SAR (No. 001/2024/SKL).

Y. Liu and H. Zhang (corresponding author) are with the State Key Laboratory of Internet of Things for Smart City and Department of Electrical and Computer Engineering, University of Macau, Macao, China (e-mail: yc07471@connect.um.edu.mo; hczhang@um.edu.mo).

D. Xie is with Institute of Catastrophe Risk Management, Nanyang Technological University, Singapore (e-mail: xied0005@e.ntu.edu.sg).

DOI: 10.35833/MPCE.2024.000067

power, typhoons primarily affect two system components: ① renewable energy sources such as offshore wind farms, and ② transmission line systems. To evaluate the typhoon impact on offshore wind farms, [9] performed weather-research simulations to forecast the failure rates of offshore wind turbines. Similarly, [10] analyzed the feasibility of wind turbine under stochastic weather conditions. With respect to vulnerable overhead transmission systems, [11] investigated the correlation between the weather intensity and the history failure rates of transmission lines. In [12], the tower and line fragility were modeled based on the structural and statistical analyses. Nevertheless, addressing the inherent uncertainties associated with the typhoon impact is challenging. Various optimization models, including stochastic programming [13] and robust optimization [14], have been employed to accommodate renewable energy effectively, thus mitigating the operational cost and risks. In addition, the treatment of uncertainty based on three prediction error levels (i.e., high, medium, and low levels), which was conducted in [13], is rather coarse. In [14], only the impact of a single typhoon track was considered. In addition, the robust optimization models [15], [16] with innovative uncertainty sets accounting for typhoon track uncertainties considered only load shedding in the worst-case scenarios, which is over-conservative.

The above-mentioned studies have primarily emphasized the steady-state operation of power systems under extreme weather conditions, paying less attention to the frequency stability of a power system. After a generation-load power imbalance caused by contingencies during a typhoon, uncontrolled frequency fluctuation might lead to emergent load shedding and generation loss [17]. In [18], the frequency controls of wind farms were studied in addressing severe frequency contingencies. In [19], an innovative frequency criterion for optimal generator and flexible load scheduling under transmission line failure during typhoon was proposed. To enhance the resilience of a power system with offshore wind farms during a typhoon, [20] considered the frequency security requirements of the proactive unit commitment problem. Nevertheless, the aforementioned studies have not considered the operational shifts in offshore wind farms and the power disturbances arising from transmission line failures during a typhoon. In reality, the unavailability of virtual inertia and reserves from wind farms, coupled with failures in overhead transmission lines, exacerbates the frequency stability of the power system, which has often been overlooked. When a significant number of lines in a power system are damaged, the power system can become segmented into different regions with their own frequency dynamics, and using a unified frequency model for different regional frequencies might result in significant errors. Previous studies have mainly considered a predefined power disturbance such as the maximum generator output loss or a fixed percentage load increase [19], [21], [22], while the power disturbances caused by the generation-load power imbalances during grid islanding have not been discussed.

To overcome the aforementioned limitations, this study introduces a proactive unit commitment for power systems with high penetration of offshore wind power. In contrast to our previous work [23], this paper further considers the transmission line failure contingencies and addresses the associated post-fault frequency issues. The main contributions of this study can be summarized as follows.

1) A proactive unit commitment for power systems with high penetration of offshore wind power is proposed. It promotes wind power utilization and improves grid resilience during typhoons. In this study, both the steady-state operational states and the transient frequency dynamics are considered. To capture the spatial-temporal impacts of typhoon on the offshore wind farms and overhead transmission lines, representative scenarios are generated through Monte Carlo simulations, involving uncertain wind generation and topological changes during typhoons.

2) The proposed model incorporates two types of power disturbances stemming from wind farm cutoff and grid islanding (caused by transmission line failures) events. In addition, it further considers the consequences of topological alterations on system inertia and the regulating reserves within the frequency constraints. Further, the nonlinear frequency constraints are reformulated using the piece-wise linearization, and the optimization problem is modeled as a tractable scenario-based two-stage stochastic programming.

Numerical experiments show that the proposed model reduces the operational costs and improves the frequency stability of a power system during grid islanding events.

The rest of this paper is organized as follows. Section II introduces the typhoon model and explains its spatial-temporal impact on power system components. Section III describes two types of power disturbances during frequency regulation and defines frequency response constraints. Section IV introduces the proactive two-stage stochastic unit commitment model. Section V presents the case studies. Finally, Section VI summarizes our conclusions.

II. Typhoon Model and Its Spatral-temporal Impact on Power System Components

This section introduces the typhoon model, considering the empirical track and wind field models. In addition, uncertainties associated with typhoon tracks are considered through typhoon simulations. Further, the spatial-temporal impact of typhoon on crucial power system components (i.e., offshore wind farms and transmission lines) is analyzed. Finally, a scenario generation method is used to capture the stochastic nature of the wind farm cutoff and grid islanding events.

A. Typhoon Track Model

In day-ahead planning, system operators usually receive early warnings of an ongoing typhoon activity and use the current typhoon conditions obtained from the meteorological department to forecast its impacts on a power system. To model a specific typhoon track, the heading direction and translation speed are calculated using an empirical typhoon track model as [24]:

$$\Delta \ln c(t) = a_1 + a_2\psi(t) + a_3\lambda(t) + a_4 \ln c(t) + a_5\theta(t) + \varepsilon_c \quad (1)$$

$$\Delta\theta(t)=b_1+b_2\psi(t)+b_3\lambda(t)+b_4c(t)+b_5\theta(t)+b_6\theta(t-1)+\varepsilon_\theta \quad (2)$$

where $c(t)$ is the translation speed; $\theta(t)$ is the heading direction (in degrees calculated from the north) of a typhoon eye; $\psi(t)$ and $\lambda(t)$ are the latitude and longitude of the typhoon eye, respectively; ε_c and ε_θ are the residual terms obeying Gaussian distributions; and a_1-a_5 and b_1-b_6 are the fitting coefficients for each $5°\times5°$ grid in the sea.

After collecting historical data of ε_c and ε_θ, typhoon track scenarios can be generated by adding sampled prediction errors from ε_c and ε_θ to the forecasted c and θ obtained by (1) and (2), respectively. More details about the stochastic typhoon track sampling can be found in [23].

The relative intensity I related to the sea surface temperature at time t is calculated by:

$$\ln I(t+1)=d_1+d_2\ln I(t)+d_3\ln I(t-1)+d_4\ln I(t-2)+d_5S_t(t)+d_6(S_t(t+1)-S_t(t))+\varepsilon_I \quad (3)$$

where $S_t(t)$ is the sea surface temperature at time t; d_1-d_6 are the model coefficients corresponding to each $5°\times5°$ grid on the sea; and ε_I is the random error term.

To estimate the coefficients in (1)-(3), this study performs the least square fitting on historical typhoon data recorded in a 6-hour interval, which were collected from the Tropical Cyclone Center of the China Meteorological Administration [25].

B. Typhoon Wind Field Model

For a specific typhoon track, wind speeds can be estimated at different locations using the typhoon wind field model [26]. The wind speed w_{sp} at a specific location represents a function of its distance d to the typhoon eye, which can be calculated as:

$$w_{sp}=\begin{cases}KW_m(1-e^{-\alpha d}) & 0\le d\le r_{mw}\\ W_m e^{-\ln\beta\frac{d-r_{mw}}{r_s-r_{mw}}} & r_{mw}<d\le r_s\\ 0 & r_s<d\end{cases} \quad (4)$$

$$\alpha=\frac{1}{r_{mw}}\ln\frac{K}{K-1} \quad (5)$$

where W_m is the maximum wind speed; K is the typhoon speed parameter; r_{mw} is the radius corresponding to the maximum wind speed; β is the boundary parameter; and r_s is the boundary radius of the typhoon influence, where the wind speed is reduced to W_m/β.

In this study, K and β are set to be 1.14 and 10, respectively, and the estimates of the time-varying parameters W_m, r_{mw}, and r_s are obtained as [26]:

$$\ln r_{mw}=2.636-0.0005086\Delta p^2+0.0394899\psi \quad (6)$$

$$B=1.38+0.00184\Delta p-0.00309r_{mw} \quad (7)$$

$$W_m=\sqrt{B\Delta p/(\rho_{air}e)} \quad (8)$$

where B is the Holland pressure parameter; Δp is the central pressure difference; and ρ_{air} is the density of air.

Δp is associated with the relative intensity $I(t)$, which is calculated by:

$$I(t)=\frac{\Delta p}{p_{da}-p_{dc}} \quad (9)$$

where p_{da} is the surface value of the partial pressure of ambient dry air; and p_{dc} is the minimum sustainable surface value of the central pressure for a typhoon.

C. Typhoon Impact on Power System Components

Along a typhoon track, the power system components in different regions are subjected to different degrees of typhoon impacts due to the spatial-temporal wind speeds [16]. Moreover, they experience two different operational states: normal state and emergent state. For example, in the normal state, offshore wind farms provide wind power and operational reserve. However, in the emergent state, they might be cut off, causing power disturbances, and lose frequency support.

1) Offshore Wind Generation

The wind speed at the location of power system component depends on its distance to the typhoon eye, i. e., d, which can be calculated using the typhoon wind field model (4) as:

$$d=\sqrt{(\lambda_w-\lambda(t))^2+(\psi_w-\psi(t))^2} \quad (10)$$

where $(\lambda(t),\psi(t))$ is the location of typhoon eye; and (λ_w,ψ_w) is the location of power system component.

The available wind generation P^{Wa} can be obtained from the wind speed power curve as:

$$P^{Wa}=\begin{cases}0 & w_{sp}\le w_{ci}\text{ or }w_{sp}\ge w_{co}\\ \frac{1}{2}\rho_{air}C_pAw_{sp}^3 & w_{ci}<w_{sp}\le w_r\\ P_r & w_r<w_{sp}<w_{co}\end{cases} \quad (11)$$

where w_{ci}, w_{co}, and w_r are the cut-in, cutoff, and rated wind speeds, which are 3 m/s, 20 m/s, and 12 m/s, respectively; and C_p, A, and P_r are the rotor power coefficient, the blade swept area, and the rated power, respectively.

2) Failure Rate of Transmission Line

Overhead transmission lines are vulnerable to typhoons, and their failure rates are associated with wind speed, as presented in Fig. 1 [12]. Because any independent failure of the conductor segment can result in a failure of the corresponding line, the failure rate of line ij, i.e., $\pi_{ij}(t)$, can be calculated as:

$$\pi_{ij}(t)=1-\prod_{n=1}^{N_n}(1-\pi_{ij,n}(t)) \quad (12)$$

where N_n is the number of line segments; and $\pi_{ij,n}(t)$ is the failure rate of a line segment n of a line ij.

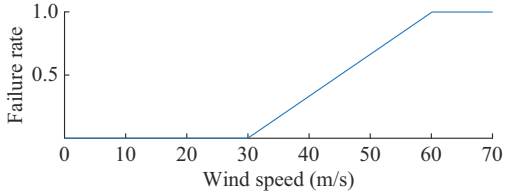

Fig. 1. Fragility curve of transmission lines under a typhoon.

D. Typhoon Scenario Generation

In day-ahead scheduling, system operators only know the initial conditions of the coming typhoon, and the trajectory of a typhoon is highly uncertain during its active period. We consider the impacts of two types of uncertainties on the power system: the long-term and the short-term uncertainties in Fig. 2. The long-term uncertainty stems from the stochastic nature of typhoon paths, encompassing the uncertainty of tracks in each scheduling period stage by stage. The short-term uncertainty refers to the uncertainty of the status of various power system components under a specific wind speed during a dispatch interval, as depicted in Fig. 2 at time t_0. The output of offshore wind farms $p_{it_0}^{\mathrm{W}}$ and the failure rate of transmission lines π_{ijt_0} are determined by wind speed. The expectation of the binary variable representing the transmission line state I_{ijt_0} is equal to π_{ijt_0}. The long-term uncertainty is addressed by considering future typhoon track scenarios through stochastic programming, while the short-term uncertainty is addressed by considering possible network topology scenarios after transmission line failures using robust optimization.

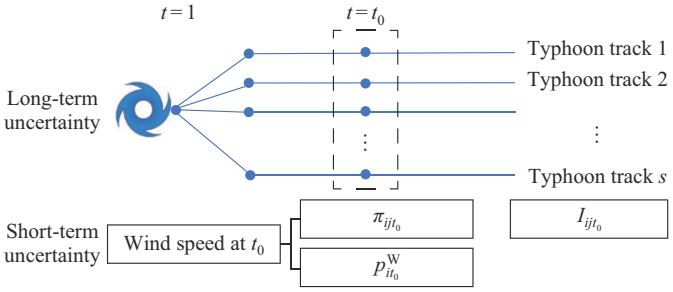

Fig. 2. Framework of two-level uncertainties.

Then, this study conducts typhoon track simulations, calculates the wind speeds at the locations of power system components, and generates scenarios for offshore wind generation and transmission line states in Monte Carlo simulations, as shown in Algorithm 1.

Algorithm 1: scenario generation for offshore wind generation and transmission line state determination under uncertainties

Input: locations of offshore wind farms and transmission lines, initial network topology, initial typhoon position, empirical formulas for the forecasted typhoon track, and prediction errors

Output: typhoon track, wind speeds at locations of power system components, available offshore wind generation, failure rates of transmission line, normal or post-fault network topology required for steady-state constraints along with their estimated probabilities, and constraints for two types of transient events (grid islanding and wind farm cutoff events): occurrence time, the topology of separated regions, and the conventional or wind units included

1: Determine the coordinates of midpoints for transmission line segments and offshore wind farms

Repeat

2: Obtain the current coordinate, translation speed, and heading direction of a typhoon, and calculate the typhoon movement in the next time step using empirical formulas (1) and (2)

3: Sample random prediction errors ε_c and ε_θ, add them to the calculated typhoon movement obtained in *Step 2*, and determine the typhoon coordinate in the next step

Until the maximum number of typhoon track samples $N_{\mathrm{track,max}}$ is reached

4: Perform scenario reduction on N_{reduced} scenarios and record the probabilities corresponding to each of the scenarios

for each reduced typhoon track numbered from 1 to N_{reduced} **do**

Repeat

for $t=1$ to T (the period of the time span) **do**

5: Determine the wind field of the current typhoon by (6)-(8), calculate distances from the typhoon eye to the power system components (i.e., wind farms and transmission lines) using (10), and obtain the corresponding wind speeds at the locations of power system components by (4) and (5)

6: For each offshore wind farm, calculate wind power output by (11), record the moment t_{windco} if the wind turbine operates at time $t_{\mathrm{windco}}-1$ but is forced to cut off at time t_{windco}

7: For each transmission line, calculate the failure rate of transimission line by (12), randomly sample π_r from a uniform distribution $U(0,1)$, and determine the transmission line state I_{ijt} as:

$$I_{ijt}=\begin{cases}0 & \pi_r\le\pi_{ij}(t)\ \text{or}\ I_{ij,t-1}=0\\ 1 & \text{otherwise}\end{cases} \tag{13}$$

8: Inspect the connectivity of the network topology after determining all transmission line statuses. If the power grid separates into multiple regions at t_{isl}, record the moment t_{isl} and the corresponding topology, and use this islanding information to analyze the frequency dynamic

end for

9: Record the network topology during period T under the current typhoon track and use it to describe the steady operational state

Until the maximum number of steady-state operational topology samples $N_{\mathrm{topology,max}}$ is reached

end for

III. Description of Power Disturbances and Frequency Response Constraints

This section first introduces the frequency dynamic model, and then derives frequency response constraints of three indices, namely rate of change of frequency (RoCoF), quasi-steady-state frequency (QSS), and frequency nadir. Subsequently, it analyzes the impact of a typhoon on the system frequency dynamics and presents two new types of power disturbances. Finally, the multi-region frequency constraints are defined considering variations in the power network topology.

A. Frequency Dynamic Model

As investigated in [19] and [22], the system-level frequency dynamics after a sudden power disturbance ΔP_{dis} can be described by a first-order ordinary differential equation as:

$$\frac{2H}{f_0}\frac{\mathrm{d}\Delta f}{\mathrm{d}t}+D\Delta f=\sum_{i\in\mathcal{I}^{\mathrm{G}}}\Delta P_i^{\mathrm{G}}+\sum_{i\in\mathcal{I}^{\mathrm{W}}}\Delta P_i^{\mathrm{W}}-\Delta P_{\mathrm{dis}} \tag{14}$$

where H, f_0, Δf, and D are the system-level inertia, nominal frequency, frequency deviation, and damping factor, respectively; $\mathcal{I}^{\mathrm{G}}$ and $\mathcal{I}^{\mathrm{W}}$ are the sets of buses equipped with a conventional generator and a wind farm, respectively; and ΔP_i^{G} and ΔP_i^{W} are the generation increments of conventional generator and wind farm after a power disturbance, respectively, representing piece-wise linear functions, which are defined as [21]:

$$\Delta P_i^{\mathrm{G}}=\begin{cases}0 & t<t_{\mathrm{DB}}\\ R_i^{\mathrm{G}}(t-t_{\mathrm{DB}})/t_{\mathrm{d}} & t_{\mathrm{DB}}\le t\le t_{\mathrm{DB}}+t_{\mathrm{d}}\\ R_i^{\mathrm{G}} & t_{\mathrm{DB}}+t_{\mathrm{d}}<t\end{cases} \tag{15}$$

$$\Delta P_i^{\mathrm{W}}=\begin{cases}0 & t<t_{\mathrm{DB}}\\ R_i^{\mathrm{W}}(t-t_{\mathrm{DB}})/t_{\mathrm{d}} & t_{\mathrm{DB}}\le t\le t_{\mathrm{DB}}+t_{\mathrm{d}}\\ R_i^{\mathrm{W}} & t_{\mathrm{DB}}+t_{\mathrm{d}}<t\end{cases} \tag{16}$$

where R_i^{G} and R_i^{W} are the reserves from the conventional generators and wind farms at bus i, respectively; and t_{DB} and t_{d} are the dead-band time and the delivery time of frequency response, respectively.

This paper considers a system aggregated inertia obtained by the sum of inertia from synchronous units and wind farms [21]. The wind turbine provides a fixed virtual inertia in pitch control mode [27]. Substituting (15) and (16) into (14) and solving it yields the following expression for frequency deviation:

$$\Delta f=\begin{cases}2\dfrac{\Delta P_{\mathrm{dis}}}{D}\left(1-\mathrm{e}^{-\frac{D}{2H}t}\right) & t<t_{\mathrm{DB}}\\ \dfrac{1}{D^2t_{\mathrm{d}}}[RD(t-t_{\mathrm{DB}})+\Delta P_{\mathrm{dis}}t_{\mathrm{d}}D-2HR]+ & \\ \left(\dfrac{2HR\mathrm{e}^{\frac{Dt_{\mathrm{DB}}}{2H}}}{T_{\mathrm{d}}D^2}-\dfrac{\Delta P_{\mathrm{dis}}}{D}\right)\mathrm{e}^{-\frac{D}{2H}t} & t_{\mathrm{DB}}\le t\le t_{\mathrm{DB}}+t_{\mathrm{d}}\end{cases} \tag{17}$$

$$R=\sum_{i\in\mathcal{I}^{\mathrm{G}}}\Delta P_i^{\mathrm{G}}+\sum_{i\in\mathcal{I}^{\mathrm{W}}}\Delta P_i^{\mathrm{W}} \tag{18}$$

$$H=\frac{1}{f_0}\left(\sum_{i\in\mathcal{I}^{\mathrm{G}}}H_i^{\mathrm{G}}P_i^{\mathrm{GU}}u_{it}^{\mathrm{G}}+\sum_{i\in\mathcal{I}^{\mathrm{W}}}H_i^{\mathrm{W}}P_i^{\mathrm{WU}}u_{it}^{\mathrm{W}}\right) \tag{19}$$

where R and H are the total system-level regulating reserve and inertia, respectively; H_i^{G} and H_i^{W} are the inertia constants of conventional generator and wind farm, respectively; P_i^{GU} and P_i^{WU} are the capacities of conventional generator and wind farm, respectively; and u_{it}^{G} and u_{it}^{W} are the on/off states of conventional generator and wind farm, respectively.

According to the frequency requirements, the RoCoF, QSS, and frequency nadir should be constrained as follows [21].

1) RoCoF Constraint

The largest RoCoF $RoCoF_{\max}$ is at the instant when a power disturbance occurs, which can be derived from (14) as:

$$\frac{1}{2}\frac{\Delta P_{\mathrm{dis}}}{RoCoF_{\max}}\le H \tag{20}$$

2) QSS Constraint

Given the frequency reaching a constant level and the full delivery of reserves, the QSS $\Delta f_{\mathrm{qss}}^{\max}$ can be derived from (14) as:

$$\Delta P_{\mathrm{dis}}-D\Delta f_{\mathrm{qss}}^{\max}\le R \tag{21}$$

3) Frequency Nadir Constraint

The frequency nadir represents the minimum value during the frequency dynamics in the interval $[t_{\mathrm{DB}},t_{\mathrm{DB}}+t_{\mathrm{d}}]$. There are mainly three models to derive the analytical frequency nadir expressions. The discretized frequency dynamic model in [28], considering speed governors, energy storage system (ESS), and load damping, can be more accurate if an appropriate time step is selected. The system frequency response (SFR) model makes some simplifications as setting similar time constants for all synchronous units and neglecting the limiters and the dead zones of the governors. Moreover, the frequency nadir expression in [29] exhibits considerable complexity and incurs a high computational burden of a mixed-integer non-linear program (MINLP) formulation, which needs further linearization. In this paper, we follow the inertia-dependent frequency model, which is easy to handle and widely adopted in many day-ahead scheduling problems [19], [21], [30]. By setting $\mathrm{d}\Delta f/\mathrm{d}t=0$ and substituting the solution into (17), the frequency nadir $\Delta f_{\mathrm{nadir}}$ can be limited as:

$$\left|\Delta f_{\mathrm{nadir}}\right|=\Delta f_{\mathrm{DB}}+\frac{\Delta P_{\mathrm{dis}}-D\Delta f_{\mathrm{DB}}}{D}+\frac{2HR}{t_{\mathrm{d}}D^2}\ln\frac{2HR}{2HR+t_{\mathrm{d}}D(\Delta P_{\mathrm{dis}}-D\Delta f_{\mathrm{DB}})}\le\Delta f_{\mathrm{nadir}}^{\max} \tag{22}$$

where Δf_{DB} is the frequency dead band; and $\Delta f_{\mathrm{nadir}}^{\max}$ is the maximum value of $\Delta f_{\mathrm{nadir}}$.

Due to the nonlinear characteristics of (22), incorporating this formula into the optimization problem poses computational challenges. In [22], a unique relationship between ΔP_{dis} and κ ($\kappa=HR$) was demonstrated. In this work, the relationship between ΔP_{dis} and κ is determined through numerical calculations $f(\kappa,\Delta P_{\mathrm{dis}})=0$:

$$f(\kappa,\Delta P_{\mathrm{dis}})=\frac{2\kappa}{t_{\mathrm{d}}}\ln\frac{2\kappa}{2\kappa+t_{\mathrm{d}}D(\Delta P_{\mathrm{dis}}-D\Delta f_{\mathrm{DB}})}-D^2(\Delta f_{\mathrm{nadir}}^{\max}-\Delta f_{\mathrm{DB}})+D(\Delta P_{\mathrm{dis}}-D\Delta f_{\mathrm{DB}}) \tag{23}$$

Then, n data points $(\Delta p_1,\kappa_1)$, $(\Delta p_2,\kappa_2)$, …, $(\Delta p_n,\kappa_n)$ are obtained, and the piece-wise linearization method is employed to approximate the mentioned relationship. As shown in Fig. 3, the curvature of the curve, which is composed of black dots, gradually increases along the horizontal axis. Finally, the conservative approximation of (22) can be obtained as:

$$\frac{\kappa_m-\kappa_{m-1}}{\Delta p_m-\Delta p_{m-1}}(\Delta P_{\mathrm{dis}}-\Delta p_{m-1})+\kappa_{m-1}\le\kappa\quad\forall m=1,2,\ldots,n \tag{24}$$

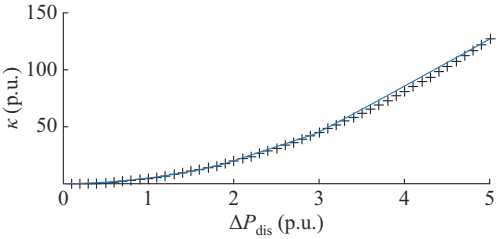

Fig. 3. Piece-wise linear fitting curves of κ and ΔP_{dis}.

It should be noted that the bilinear term HR ($\kappa=HR$) in (26) can be decomposed into multiple products of continuous and binary variables, and thus can be transformed into a mixed-integer linear programming (MILP) problem using the big-M method. In scenario s, the nadir constraints are defined as:

$$\kappa\le\frac{1}{f_0}\left(\sum_{i\in\mathcal{I}^{\mathrm{G}}}H_i^{\mathrm{G}}P_i^{\mathrm{GU}}X_{its}^{\mathrm{G}}+\sum_{i\in\mathcal{I}^{\mathrm{W}}}H_i^{\mathrm{W}}P_i^{\mathrm{WU}}X_{its}^{\mathrm{W}}\right) \tag{25}$$

$$-M(1-u_{it}^{\mathrm{G}})\le X_{its}^{\mathrm{G}}-\sum_{i\in\mathcal{I}^{\mathrm{G}}}R_{its}^{\mathrm{G}}-\sum_{i\in\mathcal{I}^{\mathrm{W}}}R_{its}^{\mathrm{W}}\le M(1-u_{it}^{\mathrm{G}})\quad\forall i\in\mathcal{I}^{\mathrm{G}} \tag{26}$$

$$-M(1-u_{its}^{\mathrm{W}})\le X_{its}^{\mathrm{W}}-\sum_{i\in\mathcal{I}^{\mathrm{G}}}R_{its}^{\mathrm{G}}-\sum_{i\in\mathcal{I}^{\mathrm{W}}}R_{its}^{\mathrm{W}}\le M(1-u_{its}^{\mathrm{W}})\quad\forall i\in\mathcal{I}^{\mathrm{W}} \tag{27}$$

$$-Mu_{it}^{\mathrm{G}}\le X_{its}^{\mathrm{G}}\le Mu_{it}^{\mathrm{G}}\quad\forall i\in\mathcal{I}^{\mathrm{G}} \tag{28}$$

$$-Mu_{its}^{\mathrm{W}}\le X_{its}^{\mathrm{W}}\le Mu_{its}^{\mathrm{W}}\quad\forall i\in\mathcal{I}^{\mathrm{W}} \tag{29}$$

where M is a large number; and X_{its}^{G} and X_{its}^{W} are the auxiliary variables for the bilinear term of conventional generator and wind farm, respectively.

B. Typhoon Impact on System Frequency Dynamic

The previous subsection has analyzed the dynamic frequency response of a power system. However, under typhoon conditions, a power system experiences significant changes in its state and operation. Previous studies have considered power disturbances under predefined conditions, e.g., the maximum generator output loss or fixed percentage load increase, but they have not addressed two types of power disturbances related to the operational state of power system.

1) Two Types of Power Disturbances Under Typhoon Conditions

This study analyzes two types of power disturbances under typhoon conditions, which result from the forced wind farm cutoff and grid islanding caused by transmission line failures. As shown in Fig. 4, the offshore wind farm in region 2 operates at time $t_{\mathrm{dis}}-1$ but is forced to cut off at a time t_{dis} due to the influence of a typhoon. This power disturbance ΔP_{disw} is modeled with the wind turbine disconnection as:

$$\Delta P_{\mathrm{disw}}=\begin{cases}\sum_{i\in\mathcal{I}^{\mathrm{w}}}p_{its}^{\mathrm{W}} & u_{its}^{\mathrm{W}}-u_{i,t+1,s}^{\mathrm{W}}=1\\ 0 & \text{otherwise}\end{cases}=\sum_{i\in\mathcal{I}^{\mathrm{w}}}p_{its}^{\mathrm{W}}(1-u_{i,t+1,s}^{\mathrm{W}}) \tag{30}$$

where p_{its}^{W} is the output of wind farm at bus i.

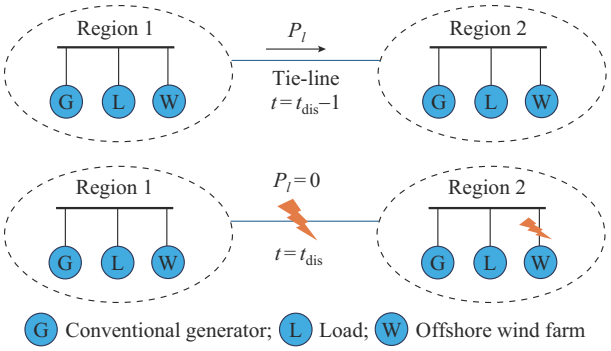

Fig. 4. Two types of power disturbances.

In Fig. 4, the tie-line functions normally at time $t_{\mathrm{dis}}-1$ but is broken at a time t_{dis} due to excessively high wind speeds, which separates the grid into two distinct regions. In each of the two regions, a power disturbance arises from the imbalance between the active power generation and the particular load demand. For example, the power disturbances in regions 1 and 2 are denoted as P_l; then, the gird islanding disturbance, ΔP_{disi}, in region r can be expressed as:

$$\Delta P_{\mathrm{disi}}=\sum_{i\in\mathcal{I}^{\mathrm{G}}\cap\mathcal{I}^{r}}p_{its}^{\mathrm{G}}+\sum_{i\in\mathcal{I}^{\mathrm{W}}\cap\mathcal{I}^{r}}p_{its}^{\mathrm{W}}+\sum_{i\in\mathcal{I}^{\mathrm{D}}\cap\mathcal{I}^{r}}(p_{it}^{\mathrm{D}}-p_{its}^{\mathrm{L}})\quad\forall r \tag{31}$$

where $\mathcal{I}^{r}$ is the set of buses in region r; $\mathcal{I}^{\mathrm{D}}$ is the sets of buses equipped with load; p_{it}^{G} is the output of conventional generator at bus i; and p_{it}^{D} and p_{its}^{L} are the load demand and load shedding at bus i, respectively.

After the grid islanding events, the frequency response resources, i.e., inertia and reserve, decrease in each separated region. When two disturbances occur simultaneously, the system response time is shorter, and there is less frequency reserve and inertia constant, resulting in more severe frequency deviations. This paper considers the worst-case scenario, where both grid islanding and wind farm cutoff events occur simultaneously, and the system must meet the frequency requirements. Combining the two aforementioned types of power disturbances, the following expression can be derived by adding (30) and (31):

$$\Delta P_{\mathrm{dis}}=\sum_{i\in\mathcal{I}^{\mathrm{G}}\cap\mathcal{I}^{r}}p_{its}^{\mathrm{G}}+\sum_{i\in\mathcal{I}^{\mathrm{D}}\cap\mathcal{I}^{r}}(p_{it}^{\mathrm{D}}-p_{its}^{\mathrm{L}})+\sum_{i\in\mathcal{I}^{\mathrm{W}}\cap\mathcal{I}^{r}}p_{its}^{\mathrm{W}}-\sum_{i\in\mathcal{I}^{\mathrm{W}}\cap\mathcal{I}^{r}}p_{its}^{\mathrm{W}}(1-u_{i,t+1,s}^{\mathrm{W}})\quad\forall r \tag{32}$$

2) Multi-region Frequency Constraints

Based on the previous analysis, the impact of a typhoon, which can cause specific overhead transmission lines to fail and result in grid islanding, initiates independent frequency response processes for each isolated region. Therefore, three different frequency indices, constrained by (20), (21), (25)-(29), must be considered individually for each isolated region. In contrast to the discussion in Section III-A, here, it is considered that the inertia and regulating reserve for each region undergo changes following the topological alteration. For region r, the inertia and regulating reserve, depending on the system topology and the corresponding RoCoF and QSS constraints, are defined as:

$$\frac{f_0\Delta P_{\mathrm{dis}}}{2\cdot RoCoF_{\max}}\le\sum_{i\in\mathcal{I}^{\mathrm{G}}\cap\mathcal{I}^{r}}H_i^{\mathrm{G}}P_i^{\mathrm{GU}}u_{it}^{\mathrm{G}}+\sum_{i\in\mathcal{I}^{\mathrm{W}}\cap\mathcal{I}^{r}}H_i^{\mathrm{W}}P_i^{\mathrm{WU}}u_i^{\mathrm{W}}\quad\forall r \tag{33}$$

$$\Delta P_{\mathrm{dis}}-D\Delta f_{\mathrm{qss}}^{\max}\le\sum_{i\in\mathcal{I}^{\mathrm{G}}\cap\mathcal{I}^{r}}\Delta P_i^{\mathrm{G}}+\sum_{i\in\mathcal{I}^{\mathrm{W}}\cap\mathcal{I}^{r}}\Delta P_i^{\mathrm{W}}\quad\forall r \tag{34}$$

The frequency nadir constraints are modified by (25)-(29), which are adjusted to the specific subset of generators and wind farms, as:

$$(25)\text{-}(29)\quad\forall i\in\mathcal{I}^{\mathrm{G}}\bigcap\mathcal{I}^{r}\text{ or }i\in\mathcal{I}^{\mathrm{W}}\bigcap\mathcal{I}^{r},\forall r \tag{35}$$

IV. Two-stage Stochastic Unit Commitment Model

This section presents the framework of the two-stage stochastic unit commitment model, as presented in Fig. 5. The proposed framework considers typhoon track uncertainties and formulates them as a two-stage stochastic problem. In the first stage, operators determine the on/off states of units, i.e., the here-and-now decisions in the day-ahead time; in the second stage, they determine adjustable generator output, reserves, and load shedding, i.e., the wait-and-see variables, to address the realized typhoon uncertainties in the real-time dispatch. On the one hand, the steady-state operational constraints denote the steady-state limitations that must be met

following a line failure and subsequent redistribution of system power. On the other hand, in scenarios where the system network is partitioned into different segments due to transmission line failures, transient constraints are necessary to ensure frequency stability in each segment.

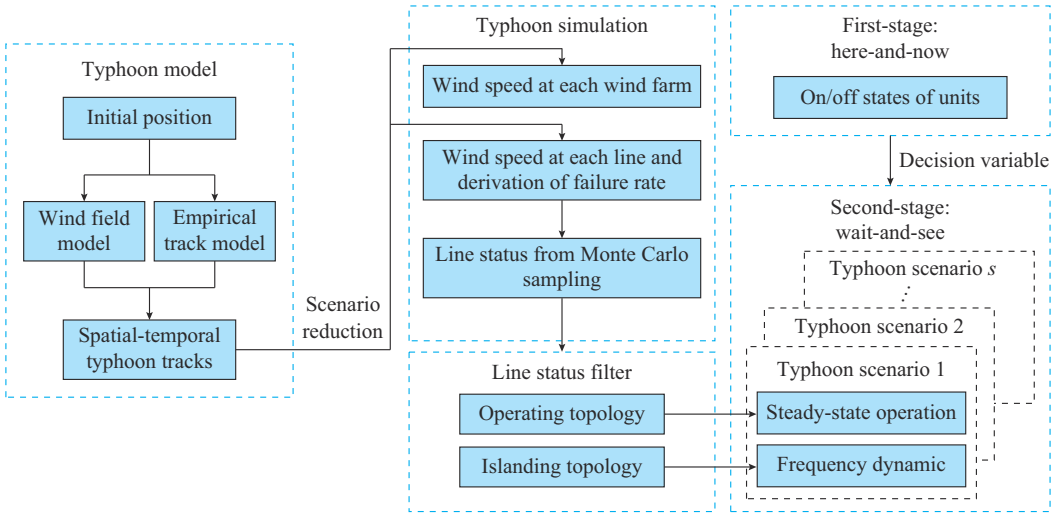

Fig. 5. Framework of two-stage stochastic unit commitment model.

A. Objective Function

The objective function of two-stage stochastic unit commitment model is defined as:

$$\min C_{\text{total}} = C_{\text{su}} + C_{\text{sd}} + C_{\text{pg}} + C_{\text{gr}} + C_{\text{wr}} + C_{\text{ls}} \tag{36}$$

$$C_{\text{su}} = \sum_t \sum_{i \in \mathcal{I}^{\text{G}}} \max\{0, c_g^{\text{u}}(u_{it}^{\text{G}} - u_{i,t-1}^{\text{G}})\} \tag{37}$$

$$C_{\text{sd}} = \sum_t \sum_{i \in \mathcal{I}^{\text{G}}} \max\{0, c_{\text{g}}^{\text{d}}(-u_{it}^{\text{G}} + u_{i,t-1}^{\text{G}})\} \tag{38}$$

$$C_{\text{pg}} = \sum_s \pi_s \sum_t \sum_{i \in \mathcal{I}^{\text{G}}} (c_{\text{g}}^0 u_{it}^{\text{G}} + c_g^1 p_{its}^{\text{G}}) \tag{39}$$

$$C_{\text{pr}} = \sum_s \pi_s \sum_t \sum_{i \in \mathcal{I}^{\text{G}}} c_{\text{gr}} R_{its}^{\text{G}} \tag{40}$$

$$C_{\text{wr}} = \sum_s \pi_s \sum_t \sum_{i \in \mathcal{I}^{\text{W}}} c_{\text{wr}} R_{its}^{\text{W}} \tag{41}$$

$$C_{\text{ls}} = \sum_s \pi_s \sum_t \sum_{i \in \mathcal{I}^{\text{D}}} c_{\text{ls}} P_{its}^{\text{L}} \tag{42}$$

where C_{total} is the total operational cost; C_{su} and C_{sd} are the start-up and shut-down costs with coefficients c_{g}^{u} and c_{g}^{d}, respectively; C_{pg} is the power generation cost with linearized coefficients c_g^0 and c_g^1; C_{gr} and C_{wr} are the reserve costs for thermal and wind generators with coefficients c_{gr} and c_{wr}, respectively; C_{ls} is the load shedding cost with coefficient c_{ls}; and π_s is the probability of the steady operational state of power system.

B. First-stage Constraints

In the first stage of the two-stage stochastic programming, the conventional generators should satisfy the following constraints:

$$\begin{cases} \sum_{t=1}^{T_i^{\text{O}}} (1 - u_{it}^{\text{G}}) = 0 \\ u_{i,0}^{\text{G}} = 1 \end{cases} \quad \forall i \in \mathcal{I}^{\text{G}} \tag{43}$$

$$T_i^{\text{U}}(u_{it}^{\text{G}} - u_{i,t-1}^{\text{G}}) \le \sum_{\tau=t}^{t+T_i^{\text{U}}-1} u_{i\tau}^{\text{G}} \quad \forall i \in \mathcal{I}^{\text{G}}, \forall t = T_i^{\text{O}}+1, T_i^{\text{O}}+2, \ldots, T - T_i^{\text{U}} + 1 \tag{44}$$

$$0 \le \sum_{\tau=t}^{T} [u_{i\tau}^{\text{G}} - (u_{it}^{\text{G}} - u_{i,t-1}^{\text{G}})] \quad \forall i \in \mathcal{I}^{\text{G}}, \forall t = T - T_i^{\text{U}} + 2, T - T_i^{\text{U}} + 3, \ldots, T \tag{45}$$

$$\begin{cases} \sum_{t=1}^{T_i^{\text{L}}} u_{it}^{\text{G}} = 0 \\ u_{i,0}^{\text{G}} = 0 \end{cases} \quad \forall i \in \mathcal{I}^{\text{G}} \tag{46}$$

$$T_i^{\text{D}}(u_{i,t-1}^{\text{G}} - u_{it}^{\text{G}}) \le \sum_{\tau=t}^{t+T_i^{\text{D}}-1} (1 - u_{i\tau}^{\text{G}}) \quad \forall i \in \mathcal{I}^{\text{G}}, \forall t = T_i^{\text{L}}+1, T_i^{\text{L}}+2, \ldots, T - T_i^{\text{D}} + 1 \tag{47}$$

$$0 \le \sum_{\tau=t}^{T} [1 - u_{i\tau}^{\text{G}} - (u_{i,t-1}^{\text{G}} - u_{it}^{\text{G}})] \quad \forall i \in \mathcal{I}^{\text{G}}, \forall t = T - T_i^{\text{D}} + 2, T - T_i^{\text{D}} + 3, \ldots, T \tag{48}$$

where T_i^{U} and T_i^{D} are the minimum up and down time, respectively; and T_i^{O} and T_i^{L} are the initial periods when the unit must be online and offline, respectively, and they are calculated by $T_i^{\text{O}} = \min\{T, (T_i^{\text{U}} - T_i^{\text{Of}}) u_{i0}^{\text{G}}\}$ and $T_i^{\text{L}} = \min\{T, (T_i^{\text{D}} - T_i^{\text{Lf}})(1 - u_{i0}^{\text{G}})\}$, and T_i^{Of} and T_i^{Lf} are the periods when the unit has been online and offline prior to the first period of the time span, respectively.

Constraints (43) - (45) denote the minimum uptime constraints in the initial T_i^{O} periods, consecutive periods of a size T_i^{U}, and the final $T_i^{\text{U}} - 1$ periods, respectively; and the minimum downtime constraints (46) - (48) are identical to (43) - (45) after the replacement of $1 - u_{it}^{\text{G}}$, T_i^{U}, and T_i^{O} with u_{it}^{G}, T_i^{D}, and T_i^{L}, respectively [31].

C. Second-stage Constraints

The second stage contains frequency constraints (33) - (35)

and steady-state operational constraints (49)-(57) (the scenario index p_{its}^{L} is omitted for brevity), which are defined as:

$$p_{it}^{\mathrm{G}}+p_{it}^{\mathrm{W}}+p_{its}^{\mathrm{L}}-p_{it}^{\mathrm{D}}=\sum_{j\in\mathcal{I}^i}p_{ijt}\quad\forall i,\forall t \tag{49}$$

$$-F_{ij}I_{ijt}\le p_{ijt}\le F_{ij}I_{ijt}\quad\forall ij,\forall t \tag{50}$$

$$-M(1-I_{ijt})\le p_{ijt}-(\theta_{it}-\theta_{jt})/X_{ij}\le M(1-I_{ijt})\quad\forall ij,\forall t \tag{51}$$

$$p_{it}^{\mathrm{G}}-p_{i,t-1}^{\mathrm{G}}\le R_i^{\mathrm{GU}}u_{i,t-1}^{\mathrm{G}}+R_i^{\mathrm{SU}}(u_{it}^{\mathrm{G}}-u_{i,t-1}^{\mathrm{G}})\quad\forall i\in\mathcal{I}^{\mathrm{G}},\forall t \tag{52}$$

$$p_{i,t-1}^{\mathrm{G}}-p_{it}^{\mathrm{G}}\le R_i^{\mathrm{GD}}u_{it}^{\mathrm{G}}+R_i^{\mathrm{SD}}(u_{i,t-1}^{\mathrm{G}}-u_{it}^{\mathrm{G}})\quad\forall i\in\mathcal{I}^{\mathrm{G}},\forall t \tag{53}$$

$$P_i^{\mathrm{GL}}u_{it}^{\mathrm{G}}+R_{it}^{\mathrm{G}}\le p_{it}^{\mathrm{G}}\le P_i^{\mathrm{GU}}u_{it}^{\mathrm{G}}-R_{it}^{\mathrm{G}}\quad\forall i\in\mathcal{I}^{\mathrm{G}},\forall t \tag{54}$$

$$0\le R_{it}^{\mathrm{G}}\le\eta P_i^{\mathrm{GU}}\quad\forall i\in\mathcal{I}^{\mathrm{G}},\forall t \tag{55}$$

$$R_{it}^{\mathrm{W}}\le p_{it}^{\mathrm{W}}\le P_{it}^{\mathrm{Wa}}-R_{it}^{\mathrm{W}}\quad\forall i\in\mathcal{I}^{\mathrm{W}},\forall t \tag{56}$$

$$0\le p_{its}^{\mathrm{L}}\le p_{it}^{\mathrm{D}}\quad\forall i\in\mathcal{I}^{\mathrm{D}},\forall t \tag{57}$$

where p_{ijt} and I_{ijt} are the power flow and operational status of a branch ij, respectively; θ_{it} is the phase angle at bus i; $\mathcal{I}^i$ is the set of buses connected to bus i; X_{ij} and F_{ij} are the reactance and capacity of branch ij, respectively; P_i^{GL} is the minimum outputs at bus i; R_i^{GU} and R_i^{GD} are the ramp-up and ramp-down limits at bus i, respectively; and R_i^{SU} and R_i^{SD} are the start-up and shut-down ramp limits at bus i, respectively.

Constraint (49) represents the power balance of a bus, and constraints (50) and (51) limit the power flow on a branch ij considering its operational status. For each conventional generator, constraints (52)-(55) ensure compliance with the specified ramp-up, ramp-down, generator output, and reserve limits, respectively. Constraint (56) describes the wind power and the reserve of a wind farm in the deloading operational mode [32]. Constraint (57) limits the maximum load shedding.

Based on the analyses presented in Sections III and IV, the two-stage stochastic unit commitment is reformulated as an MILP problem with objective (36) - (42) and constraints (43) - (48), (49) - (57), (33) - (35), which can be efficiently solved by commercial solvers, such as Gurobi [33].

V. Case Studies

The proposed frequency-constrained unit commitment is verified by case studies using the modified IEEE 5- and 30-bus systems. A predefined typhoon moves northwest, as shown in Fig. 6. Two levels of uncertainties stem from the typhoon track and the power network topology. For each typhoon track, the spatial-temporal failure rates of transmission lines are established, determining the topology scenarios for steady operational states and islanding events. To mitigate the computational burden of numerous scenarios, fifty samples of typhoon track scenarios are generated, and five scenarios (scenarios 1-5) with probabilities of 0.14, 0.28, 0.1, 0.38, and 0.1, respectively, after scenario reduction are obtained [34]. In Fig. 6, the reduced typhoon tracks 1-5 in scenarios 1-5 are indicated by cyan solid lines; and l_1-l_6 are transmission lines. In the test systems, the generator parameters are set as $H^{\mathrm{W}}=6$ s, $H^{\mathrm{G}}=4$ s, and $R_i^{\mathrm{GU}}/R_i^{\mathrm{GD}}=0.25P_i^{\mathrm{GU}}$; system parameters are set as $t_{\mathrm{d}}=10$ s, $D=0.1$ p.u., $f_0=50$ Hz, and $f_{\mathrm{DB}}=15$ mHz; frequency requirements are defined as $RoCoF_{\max}=0.2$ Hz, $\Delta f_{\mathrm{qss}}^{\max}=0.2$ Hz, and $\Delta f_{\mathrm{nadir}}^{\max}=0.5$ Hz [21].

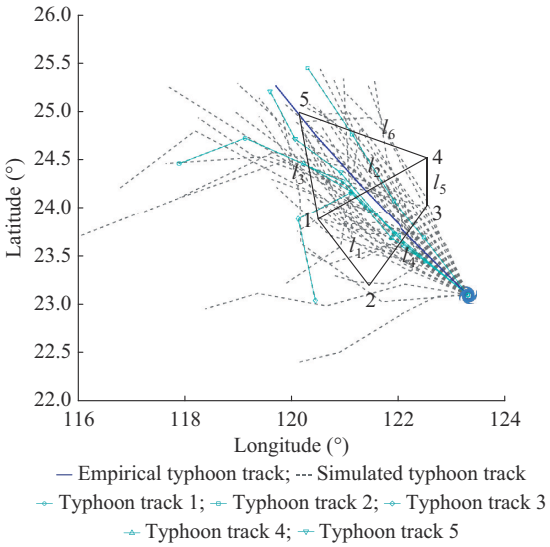

Fig. 6. Typhoon track simulation.

To verify the proposed model, the comparison are performed with the other four test models, which are introduced as follows.

1) M1: the proposed model considers two types of power disturbances with multi-region frequency constraints.

2) M2: this model considers only the wind cutoff events with unified frequency constraints while ignoring the grid islanding events.

3) M3: this model ignores frequency requirements.

4) M4: this model considers multi-region frequency constraints without virtual inertia and regulating reserve from offshore wind farms.

5) M5: this model considers multi-region frequency constraints without wind generation.

A. Modified IEEE 5-bus System

The modified IEEE 5-bus system consists of three conventional generators (G1-G3) at buses 2, 3, and 5, two offshore wind farms (W1 and W2) at buses 1 and 3, and three electricity loads at buses 2, 3, and 4 [35], respectively. The installed capacity of conventional generators is 930 MW, and the wind power penetration rate is 50%. After typhoon simulation and scenario reduction, the temporal variation of available wind generation under each typhoon track is determined, as shown in Fig. 7, and the weighted average of the line failure rates under all typhoon tracks is obtained, as presented in Fig. 8. Due to the stochastic nature of transmission line failures, 100 samples are used for each typhoon track to acquire steady operational states and record system topologies during islanding events. Table I presents reduced typhoon track and two types of power disturbances, i. e., the most frequent grid islanding and wind farm cutoff events.

1) Significance Validation of Multi-region Frequency Constraints

In this analysis, a grid islanding event under typhoon track 1 is considered. It occurs at hour 14 when the system is separated into two regions, as shown in Fig. 9.

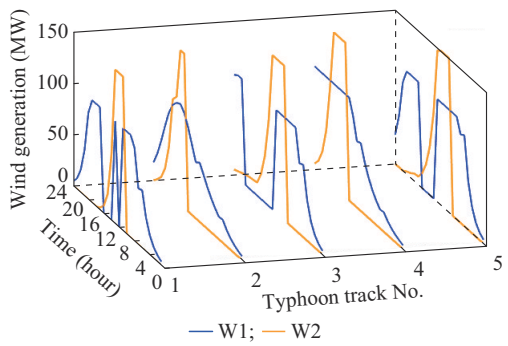

Fig. 7. Wind generation under each typhoon track.

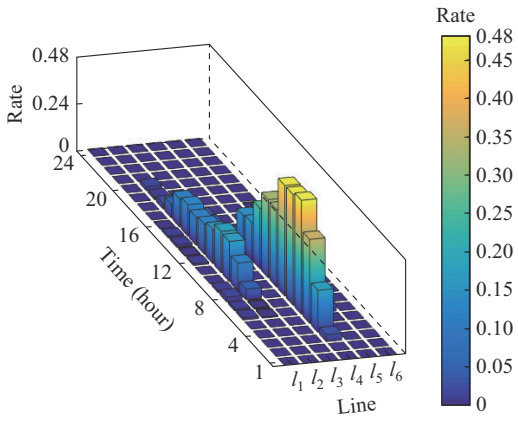

Fig. 8. Weighted average of transmission line failure rates.

After solving optimization models M1-M3, the power outputs of each generator are obtained, and the frequency indices during frequency dynamics are calculated.

TABLE I
REDUCED TYPHOON TRACK AND TWO TYPES OF POWER DISTURBANCES

Reduced typhoon track	Probability of reduced track	Number of steady operational topologies	Grid islanding		Wind farm cutoff moment (hour)	
			Most frequent topology	Moment (hour)	W1	W2
Typhoon track 1	0.14	8	[1-2], [3-5]	14, 15, 16	12, 14	18
Typhoon track 2	0.28	13	[1-2, 4-5], 3	6, 7, 8, 9, 10, 11		24
Typhoon track 3	0.10	15	[1-2], [3-5]	15, 16, 17	14	
Typhoon track 4	0.38	3	[1, 3-5], 2	12, 13		
Typhoon track 5	0.10	18	[1, 3-5], 2	6, 7, 8	14	22

Note: the symbol [] represents nodes in the same region.

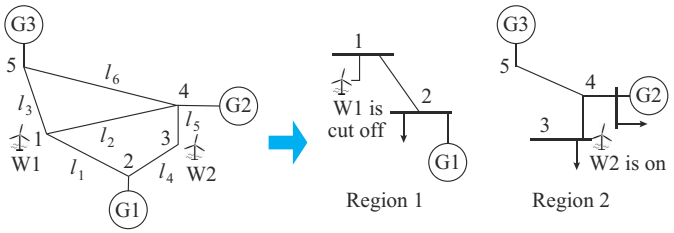

Fig. 9. Gird islanding event 1 and system topology.

The power disturbances include the power imbalance in each region and wind power curtailment from W1 in region 1. As shown in Table II, M1 could reduce the power disturbances by balancing power in each region and turning off W1 in advance. In comparison, M2 with a unified frequency in all regions considers only the cutoff disturbance in W1, while ignoring the grid islanding. As a result, although the whole system reaches a power balance, all three frequency indices in region 1 and both QSS and frequency nadir in region 2 exceed the frequency requirements. Further, M3, without frequency constraints, could handle neither grid islanding nor wind farm cutoff events, which results in more severe frequency deviations in all frequency indices in both regions.

TABLE II
SYSTEM FREQUENCY DYNAMICS OF M1-M3 UNDER GIRD ISLANDING EVENT 1

Model	Region	R (p.u.)	H (s)	ΔP_{disi} (p.u.)	ΔP_{disw} (p.u.)	RoCoF (Hz/s)	QSS (Hz)	Frequency nadir (Hz)
M1	Region 1	0	12.4	0	0	0	0	0
	Region 2	0	51.0	0	0	0	0	0
M2	Region 1	0	12.4	0.23	0	0.47	2.31	2.81
	Region 2	0	51.0	0.23	0	0.11	2.31	2.81
M3	Region 1	0	12.4	0.09	0.38	0.94	4.65	5.15
	Region 2	0	51.0	0.09	0	0.04	0.89	1.39

By considering the steady-state operation and frequency dynamics in different typhoon scenarios, the operational costs of M1-M3 are compared, as shown in Table III. The results in Table III show that M2, which neglects the grid islanding events, and M3, which lacks frequency constraints, have lower operational costs and less load shedding in the system compared with M1. This is because M1 requires more load shedding and wind power reduction in separated regions to maintain power balance. However, M2 and M3 both fail to meet the frequency requirements under the pow-

er disturbances caused by the typhoon. Table IV presents the violated scenario probability and average frequency deviations of M1-M3 in 106 power disturbances scenarios, including grid islanding and wind farm cutoff events. The results indicate that M1 has fewer scenarios with frequency deviations than other two models, and the deviations are smaller.

TABLE III
OPERATIONAL COSTS OF M1-M3

Model	Operational cost (k$)					
	Total	Start-up and shut-down of generators	Power generation	Generator reserve	Wind reserve	Load shedding
M1	499.8	0.2	285.4	1.3	1.1	211.8
M2	449.8	1.7	275.4	0.1	0.1	172.5
M3	448.7	1.7	274.6	0	0	172.4

TABLE IV
VIOLATED SCENARIO PROBABILITY AND AVERAGE FREQUENCY DEVIATIONS OF M1-M3

Model	Violated scenario probability			Average frequency deviation		
	RoCoF (%)	QSS (%)	Frequency nadir (%)	RoCoF (Hz/s)	QSS (Hz)	Frequency nadir (Hz)
M1	8	1	1	0.01	0.03	0.03
M2	70	84	84	0.70	8.69	8.00
M3	70	88	88	0.71	8.80	8.97

2) Role Validation of Offshore Wind Farms

In the power system operation, offshore wind farms not only provide active power to balance the electricity load but also offer virtual inertia and primary frequency regulation to address disturbances during a typhoon. Next, the role of wind farms is illustrated in the example of a faulty scenario under typhoon track 5. The grid islanding event occurs at hour 12 when the system is separated into three regions, as shown in Fig. 10. The power disturbances include only the power imbalance in each region since no wind farm is cut off at hour 12. To calculate three frequency indices under this event, the optimization models M1, M4, and M5 are solved, and the power disturbances, system inertia, and regulating reserve are derived, as shown in Table V. After grid islanding, region 1 experiences redundant power generation, with G3 operating at the minimum output, and all models satisfy the RoCoF requirement. M1 allocates more regulating reserves and inertia to meet the QSS and frequency requirements, whereas both M4 and M5, lacking reserves, surpass these two criteria. In region 2, M1 experiences the smallest power disturbance caused by grid islanding, with only the RoCoF value exceeding the frequency requirement. In contrast, M4 surpasses the frequency requirements for both QSS and frequency nadir; moreover, M5 fails to meet all three frequency criteria. In region 3, M1 prepares an adequate amount of frequency reserves and virtual inertia to satisfy all frequency requirements. However, in M4, the incapacity of wind turbines to provide virtual inertia leads to the RoCoF value exceeding the frequency requirements. Further, M5 meets the frequency criteria and experiences substantial load shedding due to the considerable deficit in active power, as it lacks the wind turbine output. Thus, wind turbines providing active support and virtual inertia could mitigate load shedding and enhance the frequency response performance.

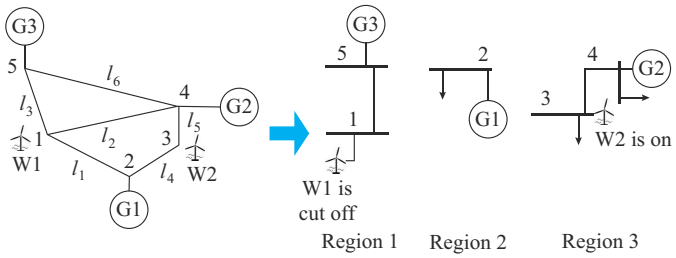

Fig. 10. Gird islanding event 2 and system topology.

TABLE V
SYSTEM FREQUENCY DYNAMICS OF MODELS UNDER GIRD ISLANDING EVENT 2

Model	Region	R (p.u.)	H (s)	ΔP_{dis} (p.u.)	RoCoF (Hz/s)	QSS (Hz)	Frequency nadir (Hz)
M1	Region 1	1.9000	22.8	0.70	0.770	0	0.0430
	Region 2	0.3100	12.4	0.29	0.590	0	0.0690
	Region 3	0.7500	51.0	0.41	0.200	0	0.0260
M4	Region 1	0	0	0.70	1.260	7.00	7.5000
	Region 2	0.3100	12.4	0.53	1.060	2.17	0.1900
	Region 3	0.4200	16.8	0.17	0.260	0	0.0250
M5	Region 1	0	0	0.70	1.570	7.00	7.5000
	Region 2	0.0025	12.4	0.68	1.370	6.75	5.2400
	Region 3	0.0025	16.8	0.02	0.033	0.20	0.0376

Amid the influence of typhoons and unpredictable system typologies, the operational costs of M1, M4, and M5, accounting for the distinct roles of wind farms, are compared, as shown in Table VI. M1 achieves the lowest operational cost among all the models. M4 could not use wind turbine reserves, resulting in higher operational costs. M5, lacking wind power and experiencing significant load shedding due to insufficient active power supply, exhibits a considerably higher operational cost. The violated scenario probability and frequency deviations of M1, M4, M5 are presented in Table VII.

TABLE VI
OPERATIONAL COSTS OF M1, M4, AND M5

Model	Operational costs (k$)					
	Total	Start-up and shut-down of generators	Power generation	Generator reserve	Wind reserve	Load shedding
M1	499.7	0.2	285.4	1.3	1.1	211.8
M4	505.6	0.2	285.4	1.6	0	218.4
M5	1259.6	0.2	372.7	0.3	0	886.4

The results indicate that M1 violates the RoCoF index slightly more than M4 and M5, and the average deviations in all frequency indices are less than those in the other two models.

TABLE VII
VIOLATED SCENARIO PROBABILITY AND AVERAGE FREQUENCY DEVIATIONS OF M1, M4, AND M5

Model	Violated scenario probability			Average frequency deviation		
	RoCoF (%)	QSS (%)	Frequency nadir (%)	RoCoF (Hz/s)	QSS (Hz)	Frequency nadir (Hz)
M1	8	1	1	0.01	0.03	0.03
M4	8	3	2	0.02	0.09	0.08
M5	3	5	8	0.03	0.15	0.15

Therefore, the offshore wind farm could leverage frequency reserves to alleviate the impact of diverse disturbances during a typhoon.

3) Sensitivity Analysis of Wind Power Penetration Rate

We compare the economic and feasibility aspects of the unit commitment model under different wind power penetration rates. Economic performance is reflected in the system operational costs, while feasibility is indicated by the penalty terms of the slack variables for load shedding and frequency deviation. As shown in Table VIII, with an increase in wind power penetration rate (keeping the capacity of conventional generators fixed and increasing the installed capacity of wind power), the total installed capacity of the system increases, and the amount of load shedding decreases. With more wind power generation, fuel consumption decreases, leading to lower operational costs. The value of the frequency deviation penalty is relatively small compared with the operational cost and is dependent on the frequency penalty cost setting (10^4 \$/Hz) [36], with little impact from the wind power penetration rate.

TABLE VIII
ECONOMIC AND FEASIBILITY ANALYSIS OF UNIT COMMITMENT MODEL UNDER DIFFERENT WIND POWER PENETRATION RATES

Penetration rate (%)	Operational cost (k$)	Load shedding cost (k$)	Frequency deviation penalty (k$)
30	723.1	379.6	4.5
40	602.7	285.3	4.2
50	504.1	214.6	5.0
60	436.1	174.2	5.4
70	392.4	151.2	3.2

B. Modified IEEE 30-bus system

The proposed model is also verified on the modified IEEE 30-bus system [37]. A typhoon is assumed to pass the test system, as shown in Fig. 11. Six conventional generators (G1-G6) are located at buses 1, 2, 22, 27, 23, and 13, and two offshore wind farms (W1 and W2) are located at buses 16 and 28, respectively. The total installed capacity of conventional generators is 198 MW. The capacities of W1 and W2 are 20 MW and 40 MW, respectively. After the typhoon simulation and scenario reduction, the steady operational state typologies and typhoon-induced wind farm cutoff and grid islanding events are obtained. The operational costs of M1-M5 are shown in Table IX, and the average frequency deviations are presented in Table X. By comparing the results in Tables IX and X, it can be observed that improper frequency constraints in M2 and M3 lead to prominent frequency deviations under typhoon-induced events. M4 exhibits slightly inferior performance to M1, which could be mainly attributed to the surplus reserves from conventional generators. Finally, M5 experiences greater load shedding and increased operational costs due to the absence of wind power generation.

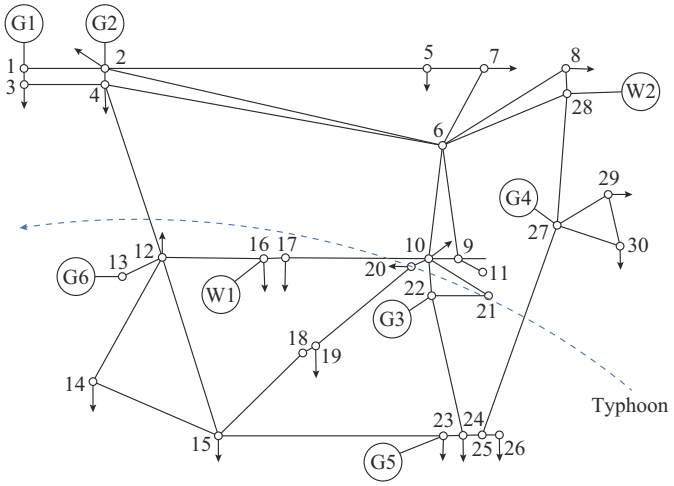

Fig. 11. Modified IEEE 30-bus system with a typhoon.

TABLE IX
OPERATIONAL COSTS OF M1-M5

Model	Operational costs (k$)					
	Total	Start-up and shut-down of generators	Power generation	Generator reserve	Wind reserve	Load shedding
M1	19.202	0.3370	9.553	0.046	0.003	9.264
M2	16.454	0.3220	9.537	0	0	6.595
M3	16.352	0.3220	9.441	0	0	6.590
M4	19.203	0.3370	9.552	0.051	0	9.264
M5	22.794	0.2367	11.010	0.066	0	11.482

TABLE X
VIOLATED SCENARIO PROBABILITY AND AVERAGE FREQUENCY DEVIATIONS OF M1-M5

Model	Violated scenario probability			Average frequency deviation		
	RoCoF (%)	QSS (%)	Frequency nadir (%)	RoCoF (Hz/s)	QSS (Hz)	Frequency nadir (Hz)
M1	4	3	5	0.04	0.01	0.02
M2	83	82	88	1.17	0.90	1.08
M3	84	83	90	1.22	0.99	1.17
M4	4	3	5	0.05	0.01	0.02
M5	4	2	5	0.05	0.01	0.02

VI. CONCLUSION

This paper proposes a two-stage stochastic unit commitment to improve the resilience of power systems integrating offshore wind energy during typhoon events. The proposed model comprehensively addresses the steady-state operation and the transient frequency dynamics under typhoon-induced

faults. The proposed model incorporates uncertainties arising from transmission line failures and offshore wind power generation through representative typhoon scenarios. The analysis includes two distinct types of power disturbances, leading to the development of innovative frequency constraints. Numerical results demonstrate the importance of accounting for grid islanding in the analysis of frequency dynamics, as well as the advantageous role of offshore wind farms in providing frequency support. In this paper, we neglect the variability of wind turbine virtual inertia under virtual synchronous machine (VSM) control parameters and instead adopt a constant inertia. In future work, we will consider more detailed frequency models, including the control strategies of power electronics converters in the voltage source converter based high-voltage DC (VSC-HVDC) transmission systems and the VSM-based wind turbines, to further explore the impact of frequency dynamics on wind turbine operation.

REFERENCES

[1] M. Li, E. Virguez, R. Shan *et al*., "High-resolution data shows China's wind and solar energy resources are enough to support a 2050 decarbonized electricity system," *Applied Energy*, vol. 306, p. 117996, Jan. 2022.

[2] P. Sherman, X. Chen, and M. McElroy, "Offshore wind: an opportunity for cost-competitive decarbonization of China's energy economy," *Science Advances*, vol. 6, no. 8, p. 9571, Feb. 2020.

[3] Y. Chen and H. Lin, "Overview of the development of offshore wind power generation in China," *Sustainable Energy Technologies and Assessments*, vol. 53, p. 102766, Oct. 2022.

[4] I. Abdin, Y.-P. Fang, and E. Zio, "A modeling and optimization framework for power systems design with operational flexibility and resilience against extreme heat waves and drought events," *Renewable and Sustainable Energy Reviews*, vol. 112, pp. 706-719, Sept. 2019.

[5] X. Dong, J. Lian, H. Wang *et al*., "Structural vibration monitoring and operational modal analysis of offshore wind turbine structure," *Ocean Engineering*, vol. 150, pp. 280-297, Feb. 2018.

[6] H. Zhang, S. Zhang, H. Cheng *et al*., "Boosting the power grid resilience under typhoon disasters by coordinated scheduling of wind energy and conventional generators," *Renewable Energy*, vol. 200, pp. 303-319, Nov. 2022.

[7] Q. Guo, Z. R. Yang, C. Liu *et al*., "Anti-typhoon yaw control technology for offshore wind farms," in *Proceedings of 2020 5th International Conference on Mechanical, Control and Computer Engineering (ICMCCE)*, Harbin, China, pp. 578-581, Dec. 2020.

[8] T. Tao, P. Shi, and H. Wang, "Spectral modelling of typhoon winds considering nexus between longitudinal and lateral components," *Renewable Energy*, vol. 162, pp. 2019-2030, Dec. 2020.

[9] L. L. Huang, Y. Fu, Y. Mi *et al*., "A Markov-chain-based availability model of offshore wind turbine considering accessibility problems," *IEEE Transactions on Sustainable Energy*, vol. 8, no. 4, pp. 1592-1600, Oct. 2017.

[10] Y. Liu, S. Li, P. W. Chan *et al*., "On the failure probability of offshore wind turbines in the China coastal waters due to typhoons: a case study using the OC4-DeepCwind semisubmersible," *IEEE Transactions on Sustainable Energy*, vol. 10, no. 2, pp. 522-532, Apr. 2019.

[11] S. Yang, W. Zhou, S. Zhu *et al*., "Failure probability estimation of overhead transmission lines considering the spatial and temporal variation in severe weather," *Journal of Modern Power Systems and Clean Energy*, vol. 7, no. 1, pp. 131-138, Jan. 2019.

[12] M. Panteli, C. Pickering, S. Wilkinson *et al*., "Power system resilience to extreme weather: fragility modeling, probabilistic impact assessment, and adaptation measures," *IEEE Transactions on Power Systems*, vol. 32, no. 5, pp. 3747-3757, Sept. 2017.

[13] X. Cai, Z. Qin, and Y. Hou, "Improving wind power utilisation under stormy weather condition by risk-limiting unit commitment," *IET Renewable Power Generation*, vol. 12, pp. 1778-1785, Sept. 2018.

[14] D. N. Trakas and N. D. Hatziargyriou, "Resilience constrained day-ahead unit commitment under extreme weather events," *IEEE Transactions on Power Systems*, vol. 35, no. 2, pp. 1242-1253, Mar. 2020.

[15] T. Zhao, H. Zhang, X. Liu *et al*., "Resilient unit commitment for day-ahead market considering probabilistic impacts of hurricanes," *IEEE Transactions on Power Systems*, vol. 36, no. 2, pp. 1082-1094, Mar. 2021.

[16] T. Ding, M. Qu, Z. Wang *et al*., "Power system resilience enhancement in typhoons using a three-stage day-ahead unit commitment," *IEEE Transactions on Smart Grid*, vol. 12, no. 3, pp. 2153-2164, May 2021.

[17] H. Ahmadi and H. Ghasemi, "Security-constrained unit commitment with linearized system frequency limit constraints," *IEEE Transactions on Power Systems*, vol. 29, no. 4, pp. 1536-1545, Jul. 2014.

[18] Z. Wu, W. Gao, T. Gao *et al*., "State-of-the-art review on frequency response of wind power plants in power systems," *Journal of Modern Power Systems and Clean Energy*, vol. 6, no. 1, pp. 1-16, Jan. 2018.

[19] Y. Yang, J. C. H. Peng, C. Ye *et al*., "A criterion and stochastic unit commitment towards frequency resilience of power systems," *IEEE Transactions on Power Systems*, vol. 37, no. 1, pp. 640-652, Jan. 2022.

[20] J. Guo, J. Zhang, T. Zhao *et al*., "Stochastic unit commitment for power systems with offshore wind farms towards frequency resiliency," *IET Renewable Power Generation*, no. 18, pp. 1218-1229, Feb. 2023.

[21] T. Ding, Z. Zeng, M. Qu *et al*., "Two-stage chance-constrained stochastic thermal unit commitment for optimal provision of virtual inertia in wind-storage systems," *IEEE Transactions on Power Systems*, vol. 36, no. 4, pp. 3520-3530, Jul. 2021.

[22] F. Teng, V. Trovato, and G. Strbac, "Stochastic scheduling with inertia-dependent fast frequency response requirements," *IEEE Transactions on Power Systems*, vol. 31, no. 2, pp. 1557-1566, Mar. 2016.

[23] Y. Liu, D. Liu, and H. Zhang, "Stochastic unit commitment with high-penetration offshore wind power generation in typhoon scenarios," *Journal of Modern Power Systems and Clean Energy*, vol. 12, no. 2, pp. 535-546, Mar. 2024.

[24] Y. Wang and D. V. Rosowsky, "Joint distribution model for prediction of hurricane wind speed and size," *Structural Safety*, vol. 35, no., pp. 40-51, 2012.

[25] CMA Tropical Cyclone Data Center. (2024, Jan.) CMA typhoon path data set. [Online]. Available: https://tcdata. typhoon.org.cn/zjljsjj_sm.html

[26] P. Javanbakht and S. Mohagheghi, "A risk-averse security-constrained optimal power flow for a power grid subject to hurricanes," *Electric Power Systems Research*, vol. 116, pp. 408-418, Nov. 2014.

[27] Z. Chu, U. Markovic, G. Hug *et al*., "Towards optimal system scheduling with synthetic inertia provision from wind turbines," *IEEE Transactions on Power Systems*, vol. 35, no. 5, pp. 4056-4066, Sept. 2020.

[28] Y. Wen, C. Y. Chung, X. Liu *et al*., "Microgrid dispatch with frequency-aware islanding constraints," *IEEE Transactions on Power Systems*, vol. 34, no. 3, pp. 2465-2468, May 2019.

[29] B. She, F. Li, H. Cui *et al*., "Virtual inertia scheduling (VIS) for real-time economic dispatch of IBR-penetrated power systems," *IEEE Transactions on Sustainable Energy*, vol. 15, no. 2, pp. 938-951, Apr. 2024.

[30] H. Yang, R. Liang, Y. Yuan *et al*., "Distributionally robust optimal dispatch in the power system with high penetration of wind power based on net load fluctuation data," *Applied Energy*, vol. 313, p. 118813, May 2022.

[31] M. Carrion and J. M. Arroyo, "A computationally efficient mixed-integer linear formulation for the thermal unit commitment problem," *IEEE Transactions on Power Systems*, vol. 21, no. 3, pp. 1371-1378, Aug. 2006.

[32] H. Li, Y. Qiao, Z. Lu *et al*., "Frequency-constrained stochastic planning towards a high renewable target considering frequency response support from wind power," *IEEE Transactions on Power Systems*, vol. 36, pp. 4632-4644, Sept. 2021.

[33] Gurobi Optimization. (2021, May). Gurobi optimizer reference manual. [Online]. Available: https://www.gurobi.com

[34] LNesp. (2024, Jan.). Scenred: code for optimal scenario tree reduction for multivariate data. [Online]. Available: https://ww2. mathworks. cn/matlabcentral/fileexchange/67909-scenred

[35] Y. Liu, Z. Li, Q. Wu *et al*., "Real-time dispatchable region of renewable generation constrained by reactive power and voltage profiles in AC power networks," *CSEE Journal of Power and Energy Systems*, vol. 6, no. 3, pp. 528-536, Sept. 2020.

[36] J. Ma, K. Summers, and F. Wen, "Joint energy and reserve market design with explicit consideration on frequency quality," *Energy Conversion and Economics*, vol. 2, pp. 25-34, Mar. 2021.

[37] M. Abdelmalak and M. Benidris, "Proactive generation redispatch to enhance power system resilience during hurricanes considering unavailability of renewable energy sources," *IEEE Transactions on Industry Applications*, vol. 58, no. 3, pp. 3044-3053, May 2022.

Yanqi Liu received the B.S. and M.S. degrees from the School of Electric Power Engineering, South China University of Technology, Guangzhou, China, in 2015 and 2020, respectively. He is currently pursuing a Ph.D. degree at the University of Macau, Macao, China. His research interests include resilience assessment, renewable energy, and integrated energy system planning and operation.

Dunjian Xie received the B.Eng and M.Sc degrees in electrical engineering from Zhejiang University, Hangzhou, China, in 2016 and 2019, respectively. He received a Ph. D. degree at Nanyang Technological University, Singapore, in 2024. Currently, he is a Postdoctoral Fellow in Nanyang Technological University and ETH Singapore Centre, Singapore. His research interests include power system resilience, stability-constrained optimization, and market analysis.

Hongcai Zhang received the B.S. and Ph.D. degrees in electrical engineering from Tsinghua University, Beijing, China, in 2013 and 2018, respectively. He is currently an Assistant Professor with the State Key Laboratory of Internet of Things for Smart City and Department of Electrical and Computer Engineering, University of Macau, Macao, China. From 2018 to 2019, he was a Postdoctoral Scholar with the Energy, Controls, and Applications Lab at University of California, Berkeley, USA, where he was a Visiting Student Researcher in 2016. His current research interests include Internet of Things for smart energy, optimal operation and optimization of power and transportation systems, and grid integration of distributed energy resources.